Available online at www.sciencedirect.com
SCIENCE DIRECT®
Journal of Nuclear Materials 349 (2006) 235–250
journal of nuclear materials
www.elsevier.com/locate/jnucmat

Kinetic Monte Carlo simulations of radiation induced segregation and precipitation

Frédéric Soisson

Service de Recherches de Métallurgie Physique, DMN-SRMP, CEA Saclay, 91191 Gif-sur-Yvette, France

Received 27 June 2005; accepted 2 November 2005

Abstract

Kinetics of radiation induced segregation and precipitation in binary alloys are studied by Monte Carlo simulations. The simulations are based on a simple atomic model of diffusion under electron irradiation, which takes into account the creation of point defects, the recombination of close vacancy–interstitial pairs and the point defect annihilation at sinks. They can reproduce the coupling between point defect fluxes towards sinks and atomic fluxes, which controls the segregation tendency. In pure metals and ideal solid solutions, the Monte Carlo results are found to be in very good agreement with classical models based on rate equations. In alloys with an unmixing tendency, we show how the interaction between the point defect distribution, the solute segregation and the precipitation driving force can generate complex microstructural evolutions, which depend on the very details of atomic-scale diffusion properties.

PACS: 61.80.x; 61.80.Az; 61.82.Bz; 64.75.+g

1. Introduction

Since the mid seventies, many radiation induced segregation (RIS) and precipitation (RIP) phenomena have been observed in model alloys or in structural materials of nuclear reactors (see e.g. Ref. [1] for a review of the major experimental results). At the atomic scale, the origin of RIS and RIP is relatively well understood: they result from the coupling between the fluxes of point defects created by the irradiation and chemical species fluxes [2–6]. A quantitative prediction of segregation and precipitation kinetics requires a precise description of the point defect jump mechanisms which control the coupling. With the usual models, based on generalized diffusion equations, the latter is often quite difficult, mainly because of the correlations between successive point defect jumps. Atomistic kinetic Monte Carlo (AKMC) simulations, based on point defect diffusion model under irradiation, can avoid this difficulty, because they naturally involve correlations effects. Our main objective is to show that such simulations, if they include non-conservative point defects and the necessary irradiation events, can offer an alternative tool to study RIS and RIP phenomena. We focus on the case of substitutional

E-mail address: fsoisson@cea.fr

0022-3115/$ - see front matter © 2005 Elsevier B.V. All rights reserved.
doi:10.1016/j.jnucmat.2005.11.003

binary solid solutions A–B with an unmixing tendency. Rather than to model a specific system, we try to develop the simplest possible model which takes into account the essential RIS and RIP mechanisms, in order to show how the details of diffusion properties control the kinetic pathway of the alloy under irradiation. Therefore, we restrict ourselves to electron irradiation conditions, where the point defect creation mechanism is more simple than under ion irradiation and we ignore more complicated effects (displacement cascades, point defect clustering, etc.) which can also affect the segregation and precipitation processes.

After a brief description of radiation damage and diffusion mechanisms which induce RIS and RIP phenomena, we present existing models and we emphasize their main advantages and drawbacks by comparison with AKMC simulations (Section 2). The atomistic diffusion model and the Monte Carlo algorithm we use are described in Section 3. The AKMC simulations are then applied to model situations of increasing complexity: in Section 4 the evolution of point defect concentrations in pure metals; in Section 5 segregation in ideal solid solutions (two cases for which classical models are reliable); and in Section 6, segregation and precipitation in alloys with an unmixing tendency. Finally, we discuss the limitations of our approach and the improvements which should be made in order to model specific alloys.

2. Radiation induced segregation and precipitation mechanisms

2.1. Radiation damage

In metallic materials, radiation damage is mainly due to elastic collisions between the incident particles and the atoms of the irradiated material, which result in the formation of point defects and point defect clusters. During an irradiation with light particles (e.g. electrons), Frenkel pairs are created in a homogeneous manner in the target. On the contrary, with heavier particles (heavy ions or neutrons), vacancies and interstitials are created in a very inhomogeneous way, in displacements cascades which have been extensively studied by molecular dynamics [7,8]. Within a few picoseconds, hundreds or thousands of defects are created in an area of few nanometers, but most of them undergo recombination or clustering very rapidly. After typically 100 ps, only a few clusters (vacancy or interstitial loops, stacking fault tetrahedra) and a few isolated point defects remain which can migrate by thermally activated jumps during longer times.

As a result, point defect concentrations under irradiation can exceed the equilibrium concentrations by several orders of magnitude. Excess point defects tend to migrate towards point defects sinks (free surfaces, grain boundaries, dislocations, etc.), where they can annihilate. Usually point defects migrate by exchanging with the various chemical elements with different frequencies: this results in a redistribution of chemical elements in the vicinity of the sinks, i.e. in the RIS phenomena.

Some empirical rules have been proposed from experimental observations [1,4,6]: e.g. in binary alloys with a strong size effect, one observes in most cases an enrichment of undersized atoms and a depletion of oversized ones near the sinks. Some simple cases can be explained by inverse Kirkendall effect: a flux of defects requires a flux of atoms, in the same direction for interstitials, in the opposite direction for vacancies. Therefore, the concentration of the elements which diffuse more rapidly as interstitials, of more slowly with vacancies, will tend to increase near the sinks. Bonds between defects and solute or solvent atoms can also play a role: if a point defect is strongly bound to a chemical element, it can drag it towards the sinks [4,9].

2.2. Diffusion equations

It is often difficult to predict the segregation tendency which results from the competition between these various mechanisms. Most of the models which have been proposed are based on generalized Fick's equations. In a dilute binary A–B alloy the evolution of the local vacancy (C_V), interstitial (C_I) and solute (C_B) concentrations, is written as

$$\begin{aligned}\frac{\partial C_V}{\partial t} &= G - RC_I C_V - \operatorname{div}\mathbf{J}_V,\\ \frac{\partial C_I}{\partial t} &= G - RC_I C_V - \operatorname{div}\mathbf{J}_I,\\ \frac{\partial C_B}{\partial t} &= -\operatorname{div}\mathbf{J}_B,\end{aligned} \tag{1}$$

where G is the point defect creation rate and R a recombination coefficient. Annihilation at sinks is taken into account by imposing local equilibrium concentrations $C_V = C_V^{eq}$ and $C_I = C_I^{eq}$ on each sink. The relations between the fluxes $\mathbf{J}_V$, $\mathbf{J}_I$, $\mathbf{J}_B$ and the concentration gradients ∇C_V, ∇C_I, ∇C_B involve several coupling coefficients which control the sign, the

magnitude and the kinetics of segregation [10]. Unfortunately, it is everything but trivial to determine the relations between the coupling coefficients and the point defect jump frequencies, mainly because of the correlation effects between successive jumps. This has been done indeed only for few simple cases: ideal solid solutions [3,5] or dilute binary alloys with special assumptions in order to limit the number of jump frequencies to consider (see Murphy for BCC alloys [11], Barbu and Lidiard for FCC alloys [12]).

In other cases, especially for concentrated alloys, phenomenological diffusion models such as the one of Manning must be used. These models do not take into account all the correlation effects and the binding energies between solute atoms and point defects [10,13].

The other main drawback of diffusion equations is that they only give the segregation kinetics, not the precipitation ones. Such deterministic descriptions do not involve thermal fluctuations which control the nucleation processes. As a consequence, the precipitation can only be predicted in a very simplified way: e.g. by supposing that it occurs instantaneously at locations where the solute concentration reaches the equilibrium solubility limit. Nucleation kinetics in super-saturated solid solutions are then especially difficult to study.

2.3. Lattice mean-field methods

Mean-field models are more suited to the study of concentrated and multicomponent alloys: they have been successfully applied for example to RIS kinetics in Ni–Cu [14] and Fe–Ni–Cr [15,16] alloys. They are based on a diffusion model on rigid lattice where the activation energies of point defect jumps are computed as a sum of broken bonds, using a mean-field approximation. They can reproduce the dependence of the jump frequencies on the local environment and then give a better description of coupling between fluxes. However they are limited by their mean-field approximation and by their treatment of correlation effects. The former point can in principle be easily improved by using a higher order approximation (e.g. a pair or a Cluster Variation Method instead of a simple point approximation [17]). The correlations are more difficult to handle: new self-consistent mean-field methods are under development [18] and could be soon applied to alloys under irradiation. However such methods are more suited to growth and coarsening than to nucleation problems, again because they do not take into account thermal fluctuations.

2.4. Atomistic kinetic Monte Carlo simulations

The same kind of atomistic diffusion model can be handled by kinetic Monte Carlo simulations. In the limited framework of a rigid lattice approximation, space and time correlations – and then thermal fluctuations – are naturally and exactly taken into account, in a finite size system (with typically 10^6–10^7 atoms), at the cost of much more CPU time. Atomistic kinetic Monte Carlo (AKMC) methods have been extensively used to study phase transformation kinetics during thermal ageing and the influence of diffusion properties, at the atomic scale, on the kinetic pathways [19–22]. In alloys under irradiation, they have been mainly used to study phase transformations controlled by ballistic mixing (dissolution of precipitates, inverse coarsening, disordering of intermetallic compounds, etc. [23]), using simplified diffusion models which did not explicitly take into account the creation, recombination and annihilation at sinks of point defects. Recently Rottler et al. have presented AKMC simulations involving these mechanisms to study the evolution of point defect concentrations in pure BCC metals [24]. They have especially introduced an interstitial model which takes into account rotations between $\langle 1\,1\,1\rangle$ directions, in order to study the effects of the competition between 1D and 3D dumbbell migration. In a previous short paper, we have started to develop a similar model (with a simpler interstitial model) to study RIS and RIP phenomena in supersaturated solid solutions [25]: we present here a more detailed study, for both under and supersaturated solid solutions, which emphasizes the control of the microstructural evolution by point defect diffusion properties.

3. Monte Carlo simulations

3.1. Atomic diffusion model

In the following, we consider binary A–B alloys on a rigid 3D lattice with a body centered cubic (BCC) structure. A and B atoms, vacancies (V) and interstitials (I) are lying on the lattice. The internal energy of the system is computed as a sum of pair interactions, between atoms (ε_{AA}, ε_{AB} and ε_{BB}) or between atoms and point defects (ε_{AV}, ε_{BV},

ε_{AI}, ε_{BI}). For the sake of simplicity, we only use first nearest neighbor pair interactions, but the model could be easily extended to pair interactions at longer range or even to multiplet interactions.

In the frame of this model, the cohesive energy of the A metal is given by: $E^{A}_{coh} = -(z/2)\varepsilon_{AA}$, the vacancy formation energy in pure A by: $E^{V}_{for}(A) = -(z/2)\varepsilon_{AA} + z\varepsilon_{AV}$ and the interstitial formation energy by: $E^{I}_{for}(A) = -(z/2)\varepsilon_{AA} + z\varepsilon_{AI}$.

Without irradiation, the equilibrium phase diagram of the A–B alloy only depends on the mixing energy $\Omega = (z/2)(\varepsilon_{AA} + \varepsilon_{BB} - 2\varepsilon_{AB})$, where $z = 8$ is the BCC lattice coordination number. If $\Omega < 0$, the system presents an unmixing tendency, with a separation between an A-rich and a B-rich phase, below the critical temperature $T_c \simeq 0.4\Omega/k_B$ [17] (k_B is the Boltzmann constant). At low temperature ($T \ll T_c$), the B solubility limit in the solid solution is given by $C^{B}_{eq} \simeq \exp(\Omega/k_B T)$.

During thermal ageing or under irradiation, kinetic properties of the A–B system are controlled by the mechanisms of creation, diffusion and elimination of point defects. The simulations include two kinds of point defects: vacancies and interstitials. In substitutional alloys, self-interstitial atoms created by irradiation are usually composed of two atoms which shared a lattice site ('dumbbell configuration'). In the model, we therefore consider three kinds of interstitial: AA, AB and BB dumbbells, as three new species lying on the BCC lattice, with no specific orientation.

The following events can occur:

1. *Frenkel pair (FP) formation:* two atoms X and Y, separated by a constant distance d_{FP}, are randomly chosen in the simulation box. A vacancy is put on the X site, a XY dumbbell on the Y site. The frequency of the FP formation is directly given, on each site, by the radiation flux G expressed in dpa s^{-1} (displacement per atom and per second). The formation of vacancies and interstitials is then homogeneous in the whole system, according to a mechanism which mimics a single replacement collision sequence (as it occurs during electron irradiation) rather than a displacement cascade.
2. *Vacancy jump:* a vacancy exchanges with a X atom (X = A or B) lying on a nearest-neighbor site, with a thermally activated jump frequency [19–23]:

$$\Gamma_{XV} = \nu_{XV} \exp[-\Delta E_{XV}/(k_B T)], \tag{2}$$

where ν_{XV} is an attempt frequency and ΔE_{XV} is an activation energy, the migration barrier, which depends on the local atomic configuration. In the frame of the rigid lattice model, ΔE_{XV} is given by

$$\Delta E_{XV} = e^{SP}_{XV} - \sum_n \varepsilon_{Xn} - \sum_p \varepsilon_{pV}, \tag{3}$$

where the sums run over the nearest-neighbor sites n of the X atom and the nearest-neighbor sites p of the vacancy. The e^{SP}_{XV} term is the interaction energy of the X atom with the surrounding atoms, when it is at the saddle-point position, during its exchange with the vacancy. For a given set of pair interactions, the choice of e^{SP}_{XV} controls the activation energy and its dependence on the local environment. In the following e^{SP}_{XV} will be either considered as a constant depending only on the nature of X, or written as a sum of effective pair interactions between the X atom and the atoms q lying on the nearest-neighbor of the saddle-point position (6 sites in the BCC structure): $e^{SP}_{XV} = \sum_q \varepsilon^{SP,V}_{Xq}$ [20].
3. *Interstitial jump:* in the same way, an interstitial I (I = AA, AB or BB) can exchange with a nearest-neighbor X atom. As for the vacancy, the jump frequency is given by

$$\Gamma_{XI} = \nu_{XI} \exp[-\Delta E_{XI}/(k_B T)], \tag{4}$$

$$\Delta E_{XI} = e^{SP}_{XI} - \sum_n \varepsilon_{Xn} - \sum_p \varepsilon_{pI} \tag{5}$$

with a saddle-point interaction energy e^{SP}_{XI} which can be taken as a constant, or depend on the local environment according to $e^{SP}_{XI} = \sum_q \varepsilon^{SP,I}_{Xq}$. Interstitial migration energies are usually smaller than vacancy ones and the e^{SP}_{XI} are chosen accordingly. After the jump the atoms which form the dumbbell can randomly dissociate or not. For example, an AB dumbbell which has exchanged with an A atom can give the following reactions: AB + A → B + AA (dissociation) or AB + A → A + AB (no dissociation), with equal probabilities.
4. *Recombination:* during their migration, when a vacancy and an interstitial become closer than the recombination distance d_{rec}, they immediately disappear by mutual recombination. One atom of the XY dumbbell is randomly chosen (e.g. X) and comes on the vacancy site, the other one (Y) stays on the initial site.
5. *Annihilation at point defect sinks:* some special lattice sites are chosen to act as perfect sinks. They can be isolated sites or they can form lines

(as a simple model for a dislocation line) or planes (as a simple model for a grain boundary). When a vacancy or an interstitial jumps onto such a site, it immediately disappears and it is replaced by a substitutional atom. The replacing atom is chosen in a 'reservoir' of matter: when a XY dumbbell annihilates on a sink site, one of the atom (e.g. X) stays on the site and the other one (Y) is stored in the reservoir. When a vacancy annihilates, it is replaced by an atom randomly chosen in the reservoir. This procedure makes it possible to keep constant the composition in the system 'simulation box + reservoir'. In practice the number of atoms stored in the reservoir is always very small by comparison with the number of atoms in the simulation box.

In order to illustrate the influence of diffusion properties on RIS and RIP kinetics, we use various sets of pair interactions and kinetic parameters (saddle-point interaction energies and attempt frequencies). However, in each case we try to choose parameters which correspond to reasonable thermodynamic and diffusion properties. For example, in pure metals the vacancy migration energies are of the order of 1 eV and the interstitial migration energies are smaller [13]. The recombination distance d_{rec} and the initial FP distance d_{FP} are typical of electron irradiations conditions, with respectively 3 and 10 nearest neighbor distances [26–28]. The kinetic have been found to be not very sensitive to the value of d_{rec} (which only slightly affects the point defect concentrations) and almost not sensitive to the one of d_{FP} (in the range $d_{\mathrm{FP}} = 5$–20 nearest neighbor distances which has been checked): therefore these two parameters are kept constant in the following.

3.2. Residence Time Algorithm

AKMC simulations have been performed on a rigid BCC lattice with typical sizes of the order of 10^6 atoms and periodic boundary conditions. The initial configuration is a random solid solution with a given composition, with no point defects.

At each Monte Carlo step, a event i is chosen with a probability proportional to its frequency Γ_i among the N possible events, using a Residence Time Algorithm (see e.g. Ref. [19]). The time corresponding to the Monte Carlo step is given by: $t_{\mathrm{MCS}} = 1/\sum_{i=1,N}\Gamma_i$. The only difference introduced by irradiation comes from instantaneous events, i.e. events which occur with an infinite frequency at soon as they are possible (recombination and annihilation at sinks). All we have to do is to look for such events at each MC step, and to perform them as soon as they are possible, without incrementing the physical time.

4. Point defect concentrations in pure metals

Before to study the kinetics of complex RIS phenomena, we have tested the behavior of our simulations in simpler situations, for which diffusion models are reliable. Let us first consider the evolution of point defects in pure metals under irradiation, to check the physical time scale and the concentrations measured in the AKMC simulations.

4.1. Rate equation and sink strengths

In a pure metal, Eq. (1) reduce to ordinary differential equations which give the evolution of average point defect concentrations [29]:

$$\begin{aligned}\frac{\mathrm{d}C_{\mathrm{V}}}{\mathrm{d}t} &= G - RC_{\mathrm{V}}C_{\mathrm{I}} - k_{\mathrm{s}}D_{\mathrm{V}}(C_{\mathrm{V}} - C_{\mathrm{V}}^{\mathrm{eq}}),\\ \frac{\mathrm{d}C_{\mathrm{I}}}{\mathrm{d}t} &= G - RC_{\mathrm{V}}C_{\mathrm{I}} - k_{\mathrm{s}}D_{\mathrm{I}}(C_{\mathrm{I}} - C_{\mathrm{I}}^{\mathrm{eq}}).\end{aligned} \tag{6}$$

All the coefficients of Eq. (6) can be directly written as a function of geometric terms and jump frequencies. The first term (G) is the irradiation flux (expressed in dpa s^{-1}). The recombination term is given by

$$R = 4\pi d_{\mathrm{rec}}\frac{D_{\mathrm{V}} + D_{\mathrm{I}}}{V_{\mathrm{at}}}, \tag{7}$$

where D_{V} and D_{I} are respectively the vacancy and interstitial diffusion coefficients in the metal (with an atomic volume $V_{\mathrm{at}} = a^3/2$ and lattice parameter a). For the vacancies: $D_{\mathrm{V}} = a^2\Gamma_{\mathrm{AV}} = a^2\nu_{\mathrm{AV}}\exp[-E^{\mathrm{V}}_{\mathrm{mig}}(\mathrm{A})/(k_{\mathrm{B}}T)]$, with a migration barrier: $E^{\mathrm{V}}_{\mathrm{mig}}(\mathrm{A}) = e^{\mathrm{SP}}_{\mathrm{AV}} - (z-1)\varepsilon_{\mathrm{AA}} - z\varepsilon_{\mathrm{AV}}$. A similar expression stands for the interstitials.

The last term of Eq. (6) corresponds to annihilations at sinks. For the time being, our simulations do not take into account the creation of equilibrium point defect in the absence of irradiation. This corresponds to: $C_{\mathrm{V}}^{\mathrm{eq}} = C_{\mathrm{I}}^{\mathrm{eq}} = 0$ (usually the equilibrium point defects concentrations are indeed very small by comparison with concentrations under irradiation and can be neglected, except at very high temperatures). The 'sink strength' k_{s} depends on the geometry and on the spatial distribution of sinks. Many studies have been devoted to the computation of sink

strengths [30,31]. For planar sinks (thin films or layers with a width e), the usual expression is

$$k_s = \frac{12}{e^2}. \tag{8}$$

For linear sinks (dislocations):

$$k_s = \frac{2\pi\rho_d}{\ln(1/\rho) - 3/4}, \tag{9}$$

where ρ_d is the dislocation density and ρ the ratio between the capture ration of point defects and the distance between dislocations. Last, for sinks with a spherical geometry:

$$k_s = 4\pi R_s C_s, \tag{10}$$

where R_s and C_s are respectively the capture radius and the concentration of the sinks.

4.2. Evolution of point defect concentrations

We have performed simulations with planar, linear and point sinks. In each case, the system contains one sink, in the center of the simulation box. The point defect concentrations are measured by time averaging and can be compared with the results of Eq. (6), where the parameters e, ρ_d and C_s of Eqs. (8)–(10) are given respectively by the width, the section and the volume of the simulation box. The following pair interactions have been used: $\varepsilon_{AA} = -1.07$ eV, $\varepsilon_{AV} = -0.30$ eV, $\varepsilon_{AI} = -0.10$ eV, which correspond to a cohesive energy $E^A_{coh} = 4.28$ eV, a vacancy formation energy $E^V_{for}(A) = 1.88$ eV and an interstitial formation energy $E^I_{for}(A) = 3.84$ eV (these values are closed to those for high purity α-iron [32]). The attempt frequencies are: $\nu_{AV} = \nu_{AI} = 5 \times 10^{15}\ s^{-1}$. The point defect migration energies are then controlled by the saddle-point interaction energies, according to $E^V_{mig} = e^{SP}_{AV} - (z-1)\varepsilon_{AA} - z\varepsilon_{AV}$ and $E^I_{mig} = e^{SP}_{AI} - (z-1)\varepsilon_{AA} - z\varepsilon_{AI}$.

We have first chosen rather high migration energies ($E^V_{mig} = 1.2$ eV and $E^I_{mig} = 0.8$ eV) which give slow kinetics, in order to highlight the first kinetics steps. Fig. 1 displays the evolution of point defect concentrations in the pure metal A, with three kinds of sinks, at $T = 400$ K and $G = 10^{-3}$ dpa s^{-1}. There is a good agreement between AKMC and diffusion equations and one observes classical kinetic behaviors which depend on the sink density [29]. With a point sink (low sink density, Fig. 1(a)) the defect concentrations increase first linearly with time ($C_I = C_V = Gt$, for $t < 10^{-2}$ s). Then a quasi steady-state is observed (with $C_I = C_V = \sqrt{G/R}$,

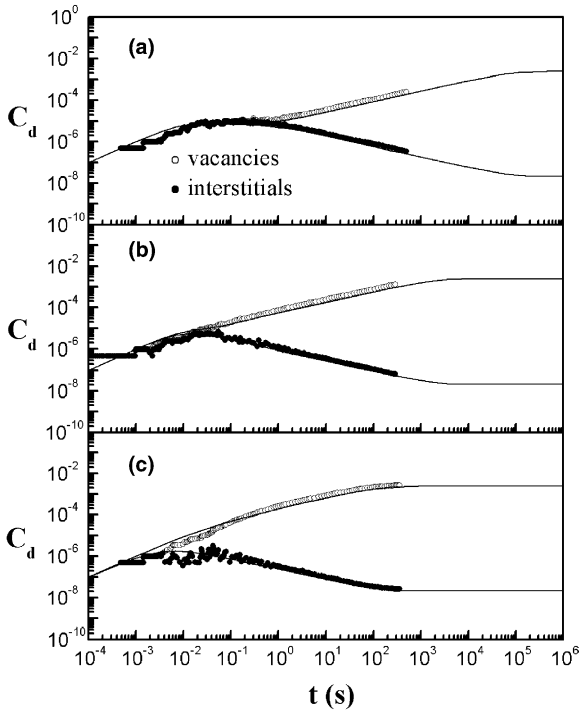

Fig. 1. Evolution of the point defect concentrations in a pure metal during irradiation at $T = 400$ K and $G = 10^{-3}$ dpa s^{-1}, with $E^V_{mig} = 1.2$ eV and $E^I_{mig} = 0.8$ eV. Simulation box with 128^3 lattice sites and one point defect sink. Effect of the sink geometry and density: (a) point sink (1 annihilation site); (b) linear sink (128 sites); (c) planar sink (128×128 sites). The symbols correspond to Monte Carlo simulations, the lines to diffusion Eq. (6).

between 10^{-2} and 1 s), where the concentrations are controlled by I/V recombinations. Interstitials are more rapid than the vacancies, so they reach the sink first: the interstitial concentration drops (at $t \simeq 1$ s), then the vacancies undergo less recombinations and their concentration increases. Finally, when at much more longer time ($t \simeq 10^5$ s), vacancies annihilate on the sink, point defect concentrations reach their steady-state values with $C^{st}_I \ll C^{st}_V$. With linear and planar sinks (Fig. 1(b) and (c)), the steady-state regime is reached at shorter times and the quasi steady-state controlled by recombinations vanishes, because of the higher density in annihilation sites.

For a given type of sink, when the migration barriers decrease (Fig. 2) or when the temperature increases, one also gets the steady-state regime much more rapidly. With smaller migration energies (e.g. $E^V_{mig} = 0.7$ eV and $E^I_{mig} = 0.35$ eV close to the estimated values in very high purity α-iron [32]), one usually observes that with the typical simulation

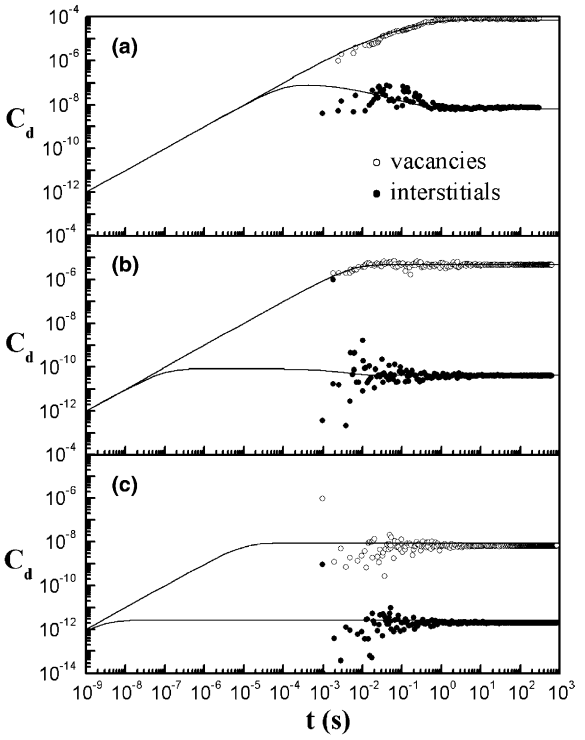

Fig. 2. Evolution of the point defect concentrations in a pure metal during irradiation at $T = 500$ K and $G = 10^{-3}$ dpa s^{-1}. Simulation box with 128^3 lattice sites and one planar point defect sink. Effect of the point defect migration energies: (a) $E^{V}_{mig} = 1.2$ eV and $E^{I}_{mig} = 0.8$ eV; (b) $E^{V}_{mig} = 1$ eV and $E^{I}_{mig} = 0.5$ eV; (c) $E^{V}_{mig} = 0.7$ eV and $E^{I}_{mig} = 0.35$ eV. The symbols correspond to Monte Carlo simulations, the lines to diffusion Eq. (6).

box sizes, as soon as it is possible to measure the point defect concentrations, they have reached their steady-state values. The typical time scale of the point defect evolution is then short compared to that of RIS and RIP processes, as we will see below.

5. Segregation kinetics: ideal solid solutions

We now consider ideal A–B solid solutions, where A and B atoms are fully miscible at every temperature, in order to study segregation kinetics without any precipitation or ordering. This can be easily achieved in the simulations by choosing pair interactions which give $\Omega = 0$. We have chosen a very simple case with $\varepsilon_{AA} = \varepsilon_{AB} = \varepsilon_{BB}$, $\varepsilon_{AV} = \varepsilon_{BV}$ and $\varepsilon_{AI} = \varepsilon_{BI}$: the point defects have then no tendency to be bond preferentially to A or B atoms. Diffusion properties are then controlled by the saddle-point interaction energies e^{SP}_{AV}, e^{SP}_{BV}, e^{SP}_{AI} and e^{SP}_{BI}, which are here chosen as constant, independent of the atomic configuration surrounding the saddle-point. With these hypothesis, the jump frequencies are different for A and B atoms, but do not depend on the local environment and the simple model developed by Wiedersich et al. to study RIS in Ni–Cu alloys can be applied [3,5]. Eq. (1) become:

$$\begin{aligned}
\frac{\partial C_V}{\partial t} &= G - RC_V C_I + \nabla[-(d_{BV} - d_{AV})C_V \nabla C_B + D_V \nabla C_V],\\
\frac{\partial C_I}{\partial t} &= G - RC_V C_I + \nabla[(d_{BI} - d_{AI})C_I \nabla C_B + D_I \nabla C_I],\\
\frac{\partial C_B}{\partial t} &= \nabla[D_B \nabla C_B + C_B(d_{BI}\nabla C_I - d_{BV}\nabla C_V)],
\end{aligned} \tag{11}$$

where the effective diffusion coefficients D_V, D_I and D_B depend on the local concentrations according to:

$$\begin{aligned}
D_V &= d_{AV}C_A + d_{BV}C_B,\\
D_I &= d_{AI}C_A + d_{BI}C_B,\\
D_B &= d_{BV}C_V + d_{BI}C_I.
\end{aligned} \tag{12}$$

The coupling between point defect and solute fluxes is then controlled by only four partial diffusion coefficients: d_{AV}, d_{BV}, d_{AI} and d_{BI}, which

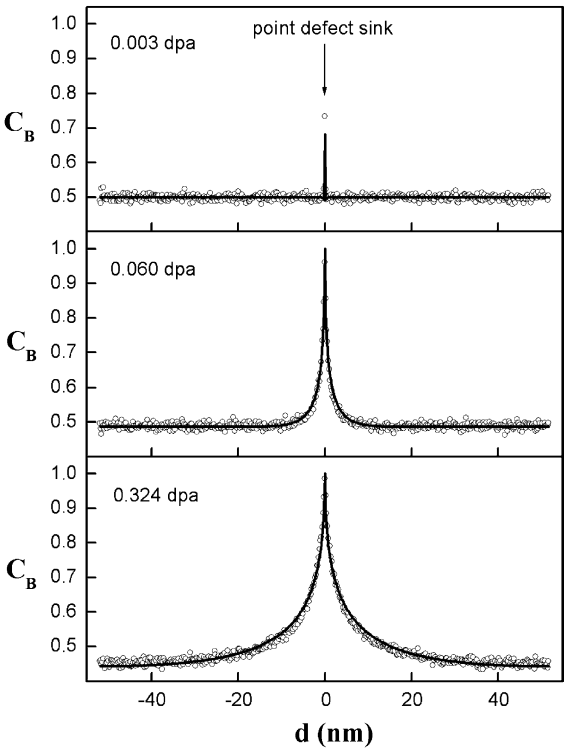

Fig. 3. Evolution of the composition profile in an $A_{50}B_{50}$ ideal solid solution under irradiation at $T = 500$ K and $G = 10^{-6}$ dpa s^{-1}. Simulation box of $512 \times 64 \times 64$ lattice sites with one planar point defect sink in the middle of the long dimension (at $d = 0$). The dots correspond to Monte Carlo simulations, the lines to the diffusion model of Eq. (11).

are directly related to the jump frequencies by: $d_{AV} = a^2 f_{AV} \Gamma_{AV}$ [3] (and similar relations for d_{BV}, d_{AI} and d_{BI}). The correlation factors f_{AV}, f_{BV}, f_{AI} and f_{BI} are estimated from the jump frequencies, using the theory of diffusion in random alloys [10,33]. For composition independent jump frequencies they remain close to one, but slightly depend on the local composition.

Figs. 3 and 4 give two examples of RIS kinetics in two A–B alloys of different compositions and for different radiation fluxes. The simulation box contains $512 \times 64 \times 64$ lattice sites, with one planar point defect sink in the middle of the longest direction. The AKMC parameters are given in Table 1. We have chosen a case where all the dumbbell interstitials have the same jump frequency ($d_{AI} = d_{BI}$) and where $\Gamma_{AV} > \Gamma_{BV}$ (i.e. $d_{AV} > d_{BV}$). The vacancy flux towards the sink induces an enrichment of slow B atoms near the sink, while the interstitial flux induces no preferential coupling and no segregation.

The composition profiles measured in AKMC simulations are very close to the ones predicted by

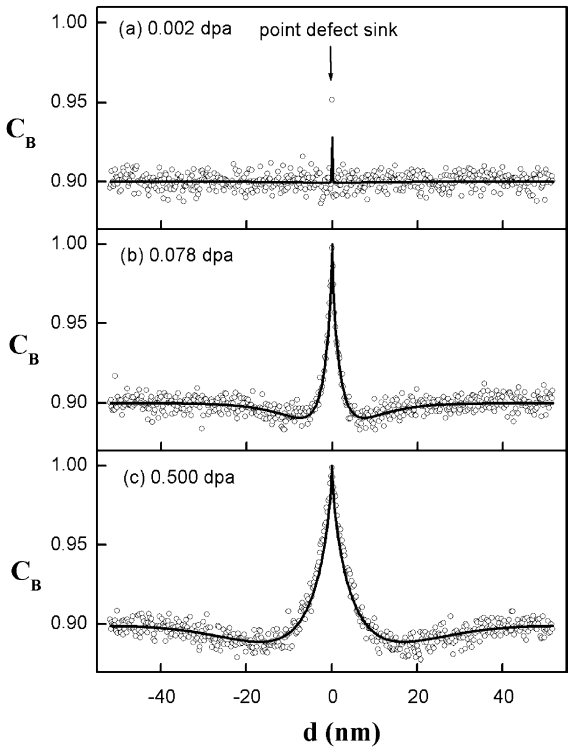

Fig. 4. Evolution of the composition profile in an $A_{10}B_{90}$ ideal solid solution under irradiation at $T = 500$ K and $G = 10^{-3}$ dpa s^{-1}. Simulation box of $512 \times 64 \times 64$ lattice sites with one planar point defect sink in the middle of the long dimension (at $d = 0$). The dots correspond to Monte Carlo simulations, the lines to the diffusion model of Eq. (11).

Table 1
AKMC parameters used for the simulations of segregation in ideal solid solution with $d_{AV} > d_{BV}$ and $d_{AI} = d_{BI}$

$\varepsilon_{AA} = \varepsilon_{AB} = \varepsilon_{BB}$	−1.07 eV
$\varepsilon_{AV} = \varepsilon_{BV}$	−0.30 eV
$\varepsilon_{AI} = \varepsilon_{BI}$	−0.10 eV
$\nu_{AV} = \nu_{BV} = \nu_{AI} = \nu_{BI}$	5×10^{15} s^{-1}
e_{AV}^{SP}	−8.89 eV
e_{BV}^{SP}	−8.79 eV
$e_{AI}^{SP} = e_{BI}^{SP}$	−7.79 eV

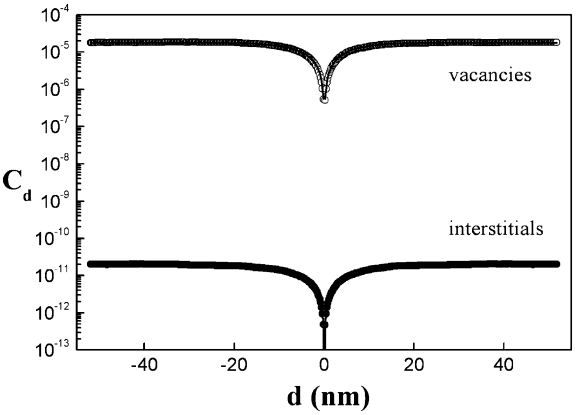

Fig. 5. Steady-state concentration profiles of point defects in a $A_{10}B_{90}$ ideal solid solution under irradiation at $T = 500$ K and $G = 10^{-3}$ dpa s^{-1}. Simulation box of $512 \times 64 \times 64$ lattice sites with one planar point defect sink in the middle of the long dimension (at $d = 0$). The dots correspond to Monte Carlo simulations, the lines to the diffusion model of Eq. (11).

numerical integration of Eq. (11), as can be seen in Figs. 3 and 4. The same agreement is observed for the point defect concentration profiles, as can be seen in Fig. 5. For high radiation fluxes ($G = 10^{-3}$ dpa s^{-1} in Fig. 4), one observes non-monotonous solute concentration profiles, typical of a non-equilibrium segregation. The particular profile of Fig. 4 corresponds typically to the one expected when $(d_{BV}/d_{AV}) < (d_{BI}/d_{AI})$ [2].

6. Precipitation kinetics

6.1. Monte Carlo parameters

The situation becomes more complex if we consider A–B regular solid solutions with a tendency to phase separation. We have used four different sets of pair interactions, attempt frequencies and saddle-point interactions (Table 2), which correspond to various thermodynamic and kinetic properties. In pure A and pure B, all these sets of

Table 2
Monte Carlo parameters used to study radiation induced precipitation in A–B alloys

Monte Carlo parameters	AKMC1 high solubility $D_B^V < D_A^V, D_B^I > D_A^I$	AKMC2 high solubility $D_B^V > D_A^V, D_B^I < D_A^I$	AKMC3 low solubility $D_B^V < D_A^V, D_B^I > D_A^I$	AKMC4 low solubility $D_B^V > D_A^V, D_B^I < D_A^I$
$\varepsilon_{AA} = \varepsilon_{BB}$	−1.070	−1.070	−1.070	−1.070
ε_{AB}	−1.043	−1.043	−0.985	−0.985
$\varepsilon_{AV} = \varepsilon_{BV}$	−0.30	−0.30	−0.30	−0.30
$\varepsilon_{AI} = \varepsilon_{BI}$	0	0	0	0
$\nu_{AV} = \nu_{BV} = \nu_{AI} = \nu_{BI}$ (s^{-1})	5×10^{15}	5×10^{15}	5×10^{15}	5×10^{15}
$\varepsilon_{AA}^{SP,V}$ (eV)	−1.481	−1.481	−1.481	−1.481
$\varepsilon_{AB}^{SP,V}$ (eV)	−1.465	−1.415	−1.382	−1.350
$\varepsilon_{BA}^{SP,V}$ (eV)	−1.415	−1.498	−1.348	−1.433
$\varepsilon_{BB}^{SP,V}$ (eV)	−1.481	−1.481	−1.481	−1.481
$\varepsilon_{AA}^{SP,I}$ (eV)	−1.165	−1.165	−1.165	−1.165
$\varepsilon_{AB}^{SP,I}$ (eV)	−1.133	−1.165	−1.048	−1.066
$\varepsilon_{BA}^{SP,I}$ (eV)	−1.165	−1.115	−1.132	−1.032
$\varepsilon_{BB}^{SP,I}$ (eV)	−1.165	−1.165	−1.165	−1.165

parameters correspond to the same cohesive energies (4.28 eV), vacancy and interstitial formation energies (1.88 and 4.28 eV), and vacancy and interstitial migration energies (1.0 and 0.5 eV). We have used a simulation box of $256 \times 64 \times 64$ lattice sites with one planar point defect sink in the middle of the longest direction.

Sets of parameters AKMC1 and AKMC2 correspond to a relatively low mixing energy ($\Omega = -0.216$ eV), which correspond to a relatively high mutual solubility limit ($C_B^{eq} \simeq 0.08$ at 800 K). It has been used to study undersaturated solid solutions, but keeping sufficient solute concentrations to get reasonable statistics.

With sets of parameters AKMC3 and AKMC4, the pair interactions give a higher mixing energy ($\Omega = -0.680$ eV): there is then almost no mutual miscibility of A and B below 1000 K ($C_B^{eq} \simeq 3.7 \times 10^{-4}$ at 1000 K and 1.4×10^{-7} at 500 K). These parameters have been used to study RIS and RIP in highly super-saturated solid solutions.

As in the previous section, the tendency for RIS of A and B atoms is controlled by the choice of saddle-point interaction energies (e_{AV}^{SP}, e_{BV}^{SP}, e_{AI}^{SP} and e_{BI}^{SP}) which determines the A and B diffusion coefficients in the alloy, by vacancy and interstitial mechanisms. But these diffusion coefficients now strongly depend on the solid solution composition, which evolves with the segregation process. It is not possible to compute the A and B diffusion coefficients in the whole composition range, but the segregation tendencies can be roughly controlled by fixing their values in pure A and B. For the vacancy mechanism, we will consider: the self-diffusion coefficients of A [$D_A^V(A)$] and B [$D_B^V(B)$], the impurity diffusion coefficient of A in B [$D_A^V(B)$] and of B in A [$D_B^V(A)$]. These four diffusion coefficients and the corresponding correlation factors have been directly computed from a small number of jump frequencies, using the theory of diffusion in dilute alloys [20,33]. Similar diffusion coefficients [$D_A^I(A)$, $D_A^I(A)$, $D_A^I(A)$ and $D_A^I(A)$] in pure A and B are considered for the interstitial mechanisms, but with the jump mechanism considered in this study, there are no available analytical relations between these coefficients and the jump frequencies: the interstitial diffusion coefficients have been directly measured by AKMC simulations in dilute solid solutions.

For the sake of simplicity, we have only considered situations where the vacancy and interstitial fluxes give the same segregation trend. Sets of parameters AKMC1 and AKMC3 correspond to a slow diffusion of B by the vacancy mechanism in pure A and in pure B [$D_B^V(A) < D_A^V(A)$ and $D_A^V(B) < D_A^V(B)$] and to a rapid diffusion of B by the interstitial mechanism [$D_B^I(A) > D_A^I(A)$ and $D_B^I(B) > D_A^I(B)$]. The two diffusion mechanisms tend to increase the B concentration near the point defect sinks, by inverse Kirkendall effect. On the contrary, with sets of parameters 2 and 4 one gets a rapid diffusion of B by the vacancy mechanism [$D_B^V(A) > D_A^V(A)$ and $D_B^V(B) > D_A^V(B)$] and a slow diffusion

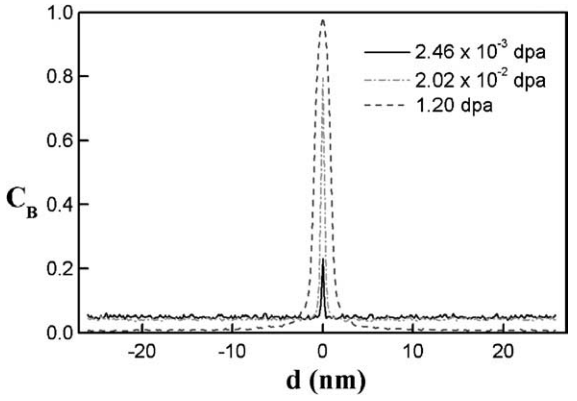

Fig. 6. Evolution of the solute concentration profile in an undersaturated A–B alloy ($C_B = 0.05$ for $C_B^{eq} = 0.08$) under irradiation at $T = 800$ K, $G = 10^{-6}$ dpa s^{-1}, in the case $D_B^V < D_A^V$ and $D_B^I > D_A^I$. Monte Carlo simulations with $256 \times 64 \times 64$ lattice sites and one planar point defect sink in the middle of the long dimension (at $d = 0$).

of B by the interstitial mechanisms $[D_B^I(A) < D_A^I(A)$ and $D_B^I(B) < D_A^I(B)]$, which both tend to decrease the B concentration near the sinks.

6.2. Undersaturated solid solutions

6.2.1. Solute Enrichment at sinks

Let us first consider simulations with the first set of parameters (AKMC1, Table 2). At $T = 800$ K, the evolution of an undersaturated solid solution (solute concentration $C_B = 0.05$, for $C_B^{eq} = 0.08$) under irradiation at $G = 10^{-6}$ dpa s^{-1}, is displayed in Figs. 6 and 7. The simulation box contains one planar point defect sink. In this alloy B solute atoms diffuse more slowly than A atoms by the vacancy mechanisms ($D_B^V/D_A^V \simeq 0.09$ in pure A and $D_B^V/D_A^V \simeq 0.33$ in pure B, at 800 K) and more rapidly by the interstitial mechanism ($D_B^I/D_A^I \simeq 18$

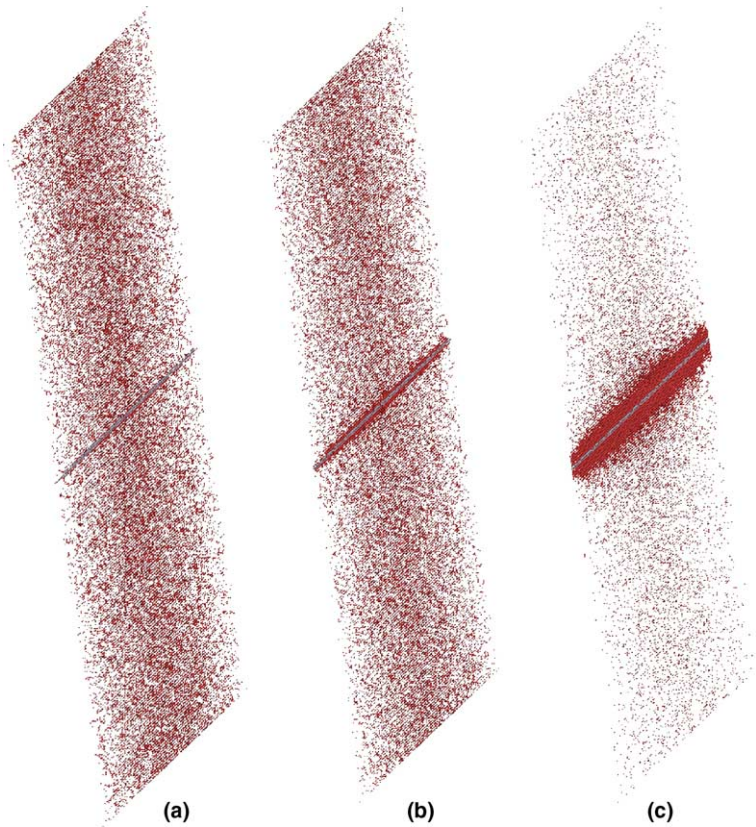

Fig. 7. Evolution of an undersaturated A–B alloy ($C_B = 0.05$ for $C_B^{eq} = 0.08$) under irradiation at $T = 800$ K, $G = 10^{-6}$ dpa s^{-1}, in the case $D_B^V < D_A^V$ and $D_B^I > D_A^I$. Microstructure at (a) 2.46×10^{-3}, (b) 2.02×10^{-2} and (c) 1.20 dpa. Monte Carlo simulations with $256 \times 64 \times 64$ lattice sites and one planar point defect sink in the middle of the long dimension. The red dots correspond to solute atoms, the blue ones to point defect sink sites.

in pure A and $D_B^I/D_A^I \simeq 1$ in pure B). In such a case, with only nearest-neighbor interaction on a BCC lattice [10,33], the flux of vacancy towards the sink drives a net flux of the rapid A atoms in the opposite direction: one observes in the simulation a strong solute enrichment on the point defect sink (Fig. 6). The solute concentration rapidly exceeds the solubility limit and precipitation starts on the sink. A continuous layer of B rich phase forms and grows as the irradiation dose increases, while the solute concentration in the matrix decreases (Fig. 7).

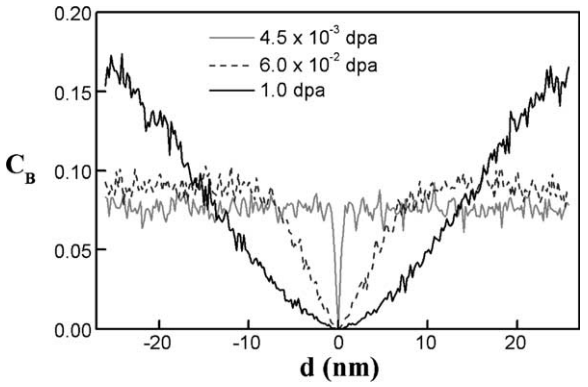

Fig. 8. Evolution of the solute concentration profile in an undersaturated A–B alloy ($C_B = 0.075$ for $C_B^{eq} = 0.08$) under irradiation at $T = 800$ K, $G = 10^{-6}$ dpa s^{-1}, for $D_B^V > D_A^V$ and $D_B^I < D_A^I$.

6.2.2. Solute depletion at sinks

In the opposite case (parameters AKMC2, Table 2), when B atoms diffuse more rapidly than A atoms by the vacancy mechanism, and more slowly by the interstitial mechanism, one observes a solute depletion near the sink. For low solute concentrations, the solid solution remains undersaturated and no precipitation occurs. However, for slightly under saturated alloys and high sink densities (Figs. 8 and 9), the solute depletion near the sinks leads to a solute enrichment far from the sinks which is sufficient to produce a beginning of precipitation far from the sinks. One example is displayed in Fig. 9 in a solid solution A–B under irradiation at 800 K and $G = 10^{-6}$ dpa s^{-1}, with $C_B = 0.075$ for $C_B^{eq} = 0.08$ (the ratio between A and B diffusion coefficients are: $D_B^V/D_A^V \simeq 3.6$ and $D_B^I/D_A^I \simeq 0.36$ in pure A, $D_B^V/D_A^V \simeq 10.7$ and $D_B^I/D_A^I \simeq 0.05$ in pure B).

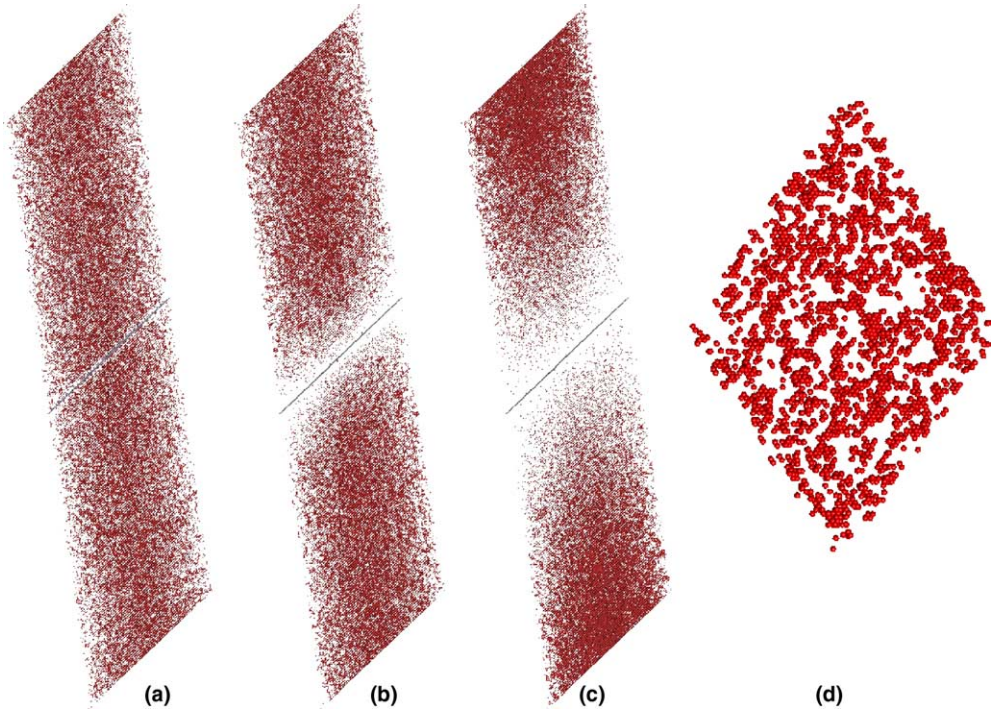

Fig. 9. Evolution of an undersaturated A–B alloy ($C_B = 0.075$ for $C_B^{eq} = 0.08$) under irradiation at $T = 800$ K, $G = 10^{-6}$ dpa s^{-1}, for $D_B^V > D_A^V$ and $D_B^I < D_A^I$. Microstructure at (a) 4.50×10^{-3}, (b) 6.0×10^{-2}, (c) and (d) 1.0 dpa. The red dots correspond to solute atoms, the blue dots to point defect sink sites. On (d), a thin slice of three atomic planes, at the very top of the simulation box is displayed: for the sake of clarity, B monomers have been omitted.

6.3. Super-saturated solid solution

6.3.1. Solute enrichment at sinks

In super-saturated solid solutions, the previous segregation tendencies are still valid, but bulk precipitation can take place and compete with segregation and precipitation at sinks. We now consider a strongly super-saturated A–B alloy with a high mixing energy (solute concentration $C_B = 0.05$, for a solubility limit $C_B^{eq} = 1.4 \times 10^{-7}$ at 500 K). The case illustrated in Figs. 10 and 11 corresponds to the set of parameters AKMC3 of Table 2 (at 500 K: $D_B^V/D_A^V \simeq 0.08$ and $D_B^I/D_A^I \simeq 5$ in A, $D_B^V/D_A^V \simeq 0.29$ and $D_B^I/D_A^I \simeq 2$ in pure B). The homogeneous precipitation and the solute enrichment at the sinks start simultaneously. Near the sink, the solute super-saturation (and therefore then, the nucleation driving force) is higher (Fig. 10(a)), but the point defect concentration (and then, the solute mobility) is lower (Fig. 10(b)). As a consequence, the precipitate growth and coarsening take place more rapidly far from the sink (Fig. 11(a) and (b)). However, at higher doses (Fig. 11(c)), the segregation leads to the formation and growth of a precipitate layer at the sink. A solute depleted and precipitate free zone is observed between the layer and the large precipitates. Finally the large precipitates which have coarsened far from the sink tend to vanish because of the continuous segregation of solute towards the sink. At the end of the sequence only the precipitate layer remains (Fig. 11(d)). We have observed that the competition between the precipitation in the bulk and at the sink, and the resulting precipitate microstructure, are very sensitive to the diffusion properties and to the super-saturation.

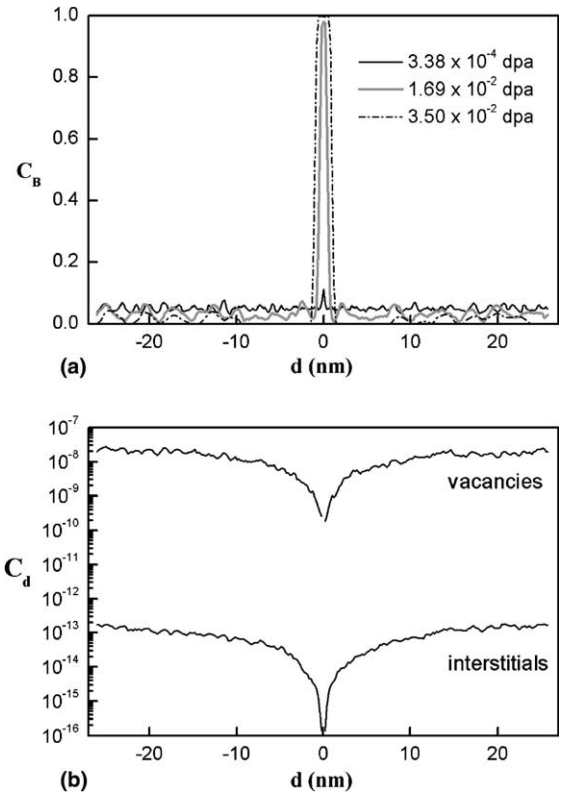

Fig. 10. (a) Evolution of the solute concentration profile and (b) point defect concentration profile at 3.38×10^{-4} dpa in a strongly super-saturated A–B alloy ($C_B = 0.05$ for $C_B^{eq} \simeq 0$) during irradiation at $T = 500$ K, $G = 10^{-6}$ dpa s^{-1} for $D_B^V < D_A^V$ and $D_B^I > D_A^I$.

6.3.2. Solute depletion at sinks

The set of parameters AKMC4 of Table 2 corresponds to a rapid diffusion of B by the vacancy mechanism (at 500 K: $D_B^V/D_A^V \simeq 8.9$ in pure A, $D_B^V/D_A^V \simeq 13.6$ in pure B) and to a slow diffusion by the interstitial mechanism (at 500 K: $D_B^I/D_A^I \simeq 0.06$ in pure A, $D_B^I/D_A^I \simeq 0.14$ in pure B). Under irradiation, the point defect flux towards the point defect sink rapidly leads to a local B depletion (Figs. 12 and 13). The phase separation process starts everywhere in the sample (Fig. 13(a)), except in the vicinity of the sink, because of the B solute depletion and of the lower point defect concentration. As the radiation dose increases (Fig. 13(b) and (c)), the growth and coarsening processes are more rapid for precipitates located far away from the sink, where the solute concentration is higher: a precipitate free zone then grows around the sink.

7. Discussion

The previous results show that AKMC simulations can be used to study qualitatively RIS and RIP phenomena in simple alloys, to rationalize the segregation and precipitation behavior as a function of the diffusion properties and to identify the main parameters which control the evolution of the microstructure.

It must be emphasized that we have considered binary BCC alloys with only first-nearest neighbor interactions. The radiation induced segregation trends are then relatively simple to understand, because they can be mainly explained in terms of inverse Kirkendall effects. For example, the solute and vacancy fluxes are always in opposite directions when the solute atoms diffuse faster than solvent atoms, because vacancy-solute complexes cannot

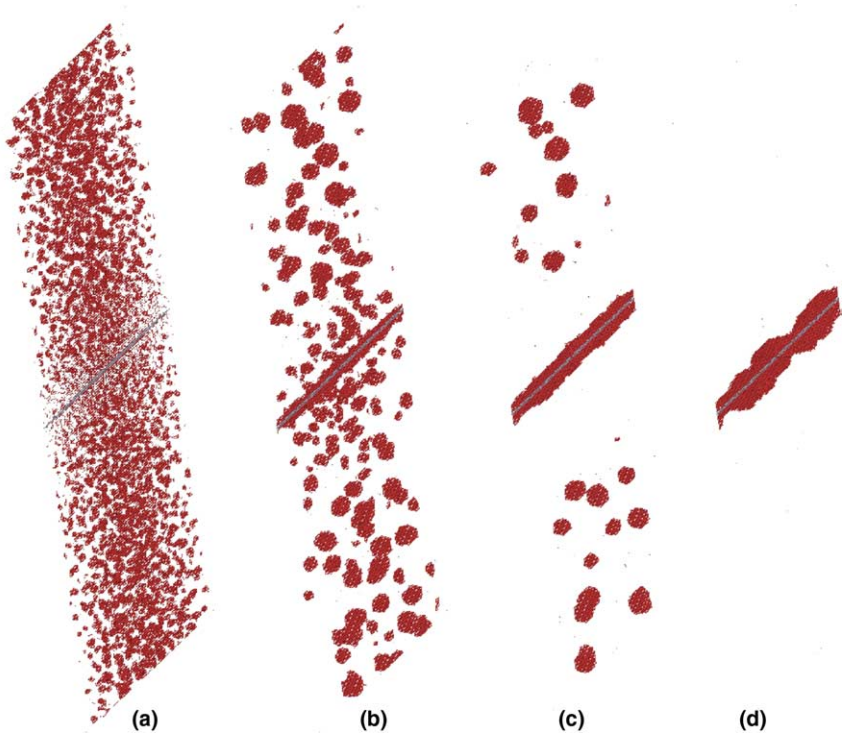

Fig. 11. Evolution of a strongly super-saturated A–B alloy ($C_B = 0.05$ for $C_B^{eq} \simeq 0$) under irradiation at $T = 500$ K, $G = 10^{-6}$ dpa s^{-1}, for $D_B^V < D_A^V$ and $D_B^I > D_A^I$. Microstructure at (a) 3.38×10^{-4} dpa, (b) 1.69×10^{-2} dpa, (c) 3.5×10^{-2} dpa and (d) 6.5×10^{-2} dpa. The red dots correspond to solute atoms, the blue dots to point defect sink sites.

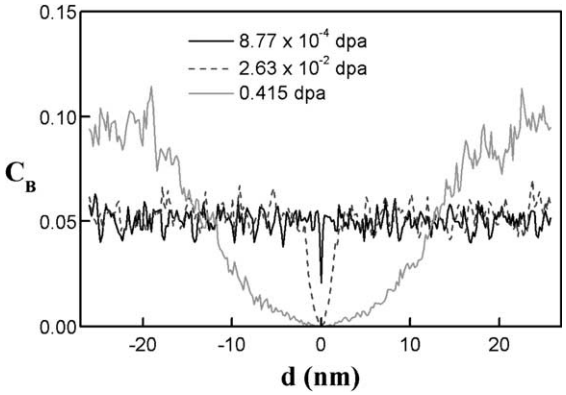

Fig. 12. Evolution of the solute concentration profile in a strongly super-saturated A–B alloy ($C_B = 0.05$ and $C_B^{eq} \simeq 0$) under irradiation at $T = 500$ K, $G = 10^{-6}$ dpa s^{-1}, for $D_B^V > D_A^V$ and $D_B^I < D_A^I$.

migrate without dissociation [12]. But it is well known that in other alloys, in case of strong binding, the vacancy can drag rapidly diffusing solute atoms towards the sinks (iron-phosphorus dilute alloys are a typical example [9]). In BCC alloys, this requires at least second-nearest neighbor interactions, which could be easily introduced in the diffusion model to deal with such situations. Nevertheless, it is worth to notice that our simulations are based on other approximations which can also affect the quantitative behavior of the system.

One of the main limitations of the present simulations lies in the interstitial model we have used. In pure metals, interstitials created under irradiation usually present relatively simple dumbbell structures [34,35]. In FCC crystals, dumbbells are usually oriented in a $\langle 1\,0\,0 \rangle$ direction and they rotate during the jump. In BCC crystals, the stable dumbbell configuration usually corresponds to a $\langle 1\,1\,0 \rangle$ orientation, but the $\langle 1\,1\,1 \rangle$ dumbbells are almost as stable, except in the case of iron where the stability difference is more important [32]. In most of the cases, migration seems to occur without rotation, which should result in a 1D or 2D interstitial diffusion. In iron, recent ab initio calculations, show a $\langle 1\,0\,0 \rangle$ dumbbell migration with rotation, which should lead to 3D interstitial diffusion [32].

In alloys, the situation is more complex: the presence of solute atoms could modify the stable configurations, or trap the dumbbells. Moreover

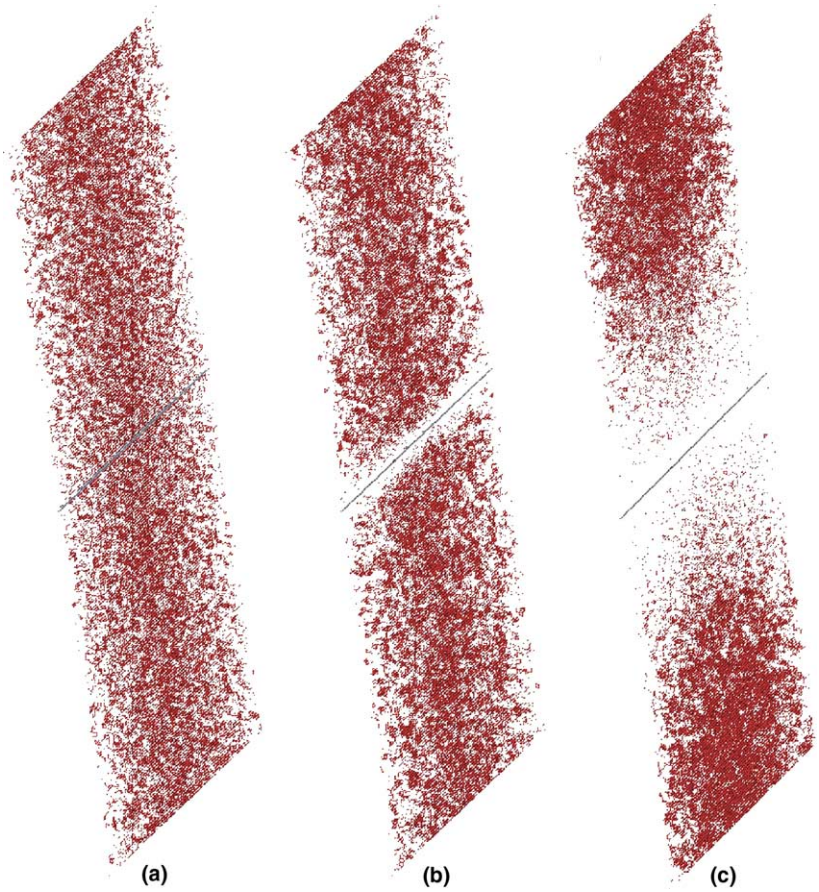

Fig. 13. Evolution of a strongly super-saturated A–B alloy ($C_B = 0.05$ and $C_B^{eq} \simeq 0$) under irradiation at $T = 500$ K, $G = 10^{-6}$ dpa s^{-1}, for $D_B^V > D_A^V$ and $D_B^I < D_A^I$. Microstructure at: (a) 8.77×10^{-4}, (b) 2.63×10^{-2} and (c) 0.415 dpa. The red dots correspond to solute atoms B, the blue ones to point defect sink sites.

mixed-dumbbell formation, with several migration, rotation and dissociation mechanisms are possible. Such features are not taken into account in our dumbbell description, but they can clearly affect the correlation effects, the diffusion properties and finally the RIS and RIP kinetic pathway under irradiation. For example the 'caging' effects which result in a dynamical trapping of mixed dumbbells in FCC alloys [34] could not be reproduced with such a simple interstitial description. Of course it is in principle quite easy to modify the dumbbell model in the simulation and to simulate such properties. This would require the introduction of new parameters (especially new activation energies, which should depend on the local atomic configuration). Unfortunately, they are very few reliable data, even in simple binary alloys, to fit these new parameters. However, one can expect that such parameters should be soon computed by new rapid ab initio calculation methods [32].

Point defects clustering can also affect the segregation and precipitation kinetics under irradiation. Such clusters can form point defects sinks, modify the point defect distributions or act as precipitate nucleus. Moreover, many molecular dynamics simulations predict that small interstitial clusters can undergo a very rapid 1D motion (at least in pure metals), which should also affect the kinetic behavior under irradiation [8,24]. For the time being, all this events are ignored in our simulations, but they could be introduced in our AKMC simulations, with the same restriction concerning the need for reliable parameters.

The formation of Frenkel pairs is also modeled in a very simple way (see Section 3.1), with small replacement collision sequences and a homogeneous production of vacancies and interstitials in the simulations box. Such a mechanism corresponds to electron irradiation conditions. To study irradiation by heavier particles, displacement

cascades could be introduced in the simulations (one could use for example the point defect and solute distributions obtained by molecular dynamics simulations).

In addition to RIS and RIP phenomena, phase transformations can also be modified or induced by ballistic mixing effects. The replacements which occur in replacement collision sequences or displacement cascades are known to produce dissolution or fragmentation of precipitates (inverse coarsening), disordering of ordered phases, etc. Such effects usually occur when the 'radiation intensity' γ, which can be defined as the ratio between ballistic and thermally activated jump frequencies, is high enough ($\gamma \sim 1$ or higher) [23]. In the simulations which have been presented here, the temperatures are relatively high and the radiation flux relatively low, so that γ always remains very small (typically: $\gamma \sim 10^{-5}$). This situation corresponds for example to the case of pressure vessels steels in nuclear power plants. However at lower temperatures or higher radiation fluxes, ballistic mixing can become predominant. For the time being, these phenomena have only been studied with AKMC simulation with conservative point defects. It is worth to mention that since the ballistic mechanisms are naturally taken into account in our simulations, they could also be used to study these problems.

8. Conclusion

AKMC simulations with creation, migration, mutual recombination and annihilation at sinks of vacancies and interstitials have been developed and applied to radiation induced segregation and precipitation kinetics in binary alloys. Despite the simplifying approximations that have been made, especially to describe the dumbbell structure and the migration of self-interstitial, they have been successfully used to model the evolution of alloys until radiation doses of typically 1 dpa. The kinetic pathway, the transient and steady-state microstructures depend on complex interactions between the segregation trend, the local point defect concentrations and the local super-saturations. Monte Carlo simulations can be used to show how the resulting evolution is controlled by the details of atomic-scale diffusion properties. Further development of the AKMC model, in connection with ab initio calculations, are planned to model specific alloys.

Acknowledgements

The author wishes to thank Alain Barbu, Emmanuel Clouet, Georges Martin and Maylise Nastar for very fruitful discussions. This work is part of the European PERFECT project and supported by the European Commission (FI60-CT-2003-508840).

References

[1] K.C. Russel, Prog. Mater. Sci. 28 (1984) 229.
[2] P.R. Okamoto, L.E. Rehn, J. Nucl. Mater. 83 (1979) 2.
[3] H. Wiedersich, P.R. Okamoto, N.Q. Lam, J. Nucl. Mater. 83 (1979) 98.
[4] L.E. Rehn, P.R. Okamoto, in: F.V. Nolfi (Ed.), Phase Transformations During Irradiation, Applied Science Publishers, London and New York, 1983, p. 247, Chapter 1.
[5] W. Wagner, L.E. Rehn, H. Wiedersich, V. Naundorf, Phys. Rev. B 28 (1983) 6780.
[6] H. Wiedersich, N.Q. Lam, in: F.V. Nolfi (Ed.), Phase Transformations During Irradiation, Applied Science Publishers, London and New York, 1983, p. 1, Chapter 1.
[7] R.S. Averback, T.D. de la Rubia, Solid State Phys. 51 (1998) 281.
[8] D.J. Bacon, F. Gao, Yu.N. Osetsky, J. Nucl. Mater. 276 (2000) 1.
[9] A.V. Barashev, Philos. Mag. 85 (2005) 1539.
[10] A.R. Allnatt, A.B. Lidiard, Atomic Transport in Solids, Cambridge University, Cambridge, 1993.
[11] S.M. Murphy, J. Nucl. Mater. 168 (1989) 31.
[12] A. Barbu, A.B. Lidiard, Philos. Mag. A 74 (1996) 709.
[13] J. Philibert, Atom Movements, Diffusion and Mass Transport in Solids, EDP Science, Les Ulis, 1991.
[14] Y. Grandjean, P. Bellon, G. Martin, Phys. Rev. B 50 (1994) 4228.
[15] M. Nastar, P. Bellon, G. Martin, and J. Ruste, in: E. Ma, M. Atzmon, P. Bellon, R. Trivedi (Eds.), Phase Transformations and Systems Driven Far From Equilibrium, Mat. Res. Soc. Symp. Proc., vol. 481, 1998, p. 383.
[16] M. Nastar, Philos. Mag. 85 (2005) 641.
[17] F. Ducastelle, Order and Phase Stability in Alloys, North-Holland, Amsterdam, 1991.
[18] M. Nastar, V.Y. Dobretsov, G. Martin, Philos. Mag. A 80 (2000) 155.
[19] F. Soisson, G. Martin, Phys. Rev. B 62 (2000) 203.
[20] Y. Le Bouar, F. Soisson, Phys. Rev. B 65 (2002) 094103.
[21] F. Soisson, in: A. Finel, D. Mazière, M. Veron (Eds.), Thermodynamics, Microstructures and Plasticity, Kluwer Academic Publishers, Dordrecht, 2003, p. 427.
[22] G. Martin, F. Soisson, in: S. Yip (Ed.), Handbook of Materials Modeling, Kluwer Academic Publishers, Dordrecht, 2005.
[23] G. Martin, P. Bellon, Solid State Phys. 50 (1997) 189.
[24] J. Rottler, D.J. Srolovitz, R. Carr, Phys. Rev. B 71 (2005) 064109.
[25] F. Soisson, Philos. Mag. 85 (2005) 489.
[26] S. Takaki, J. Fuss, H. Kugler, U. Dedek, H. Schultz, Rad. Eff. 79 (1983) 87.

[27] D.J. Bacon, A.F. Calder, F. Gao, V.G. Kapinos, S.J. Wooding, Nucl. Instrum. and Meth. B 102 (1995) 37.
[28] L.A. Zepeda-Ruiz, S. Han, D.J. Srolovitz, R. Car, B.D. Wirth, Phys. Rev. B 67 (2003) 134114.
[29] R. Sizmann, J. Nucl. Mater. 69&70 (1968) 386.
[30] F.A. Nichols, J. Nucl. Mater. 75 (1978) 32.
[31] A.D. Brailsford, R. Bullough, Philos. Trans. R. Soc. Lond. 302 (1981) 11.
[32] C.-C. Fu, F. Willaime, P. Ordejón, Phys. Rev. Lett. 92 (2004) 175503.
[33] J.-L. Bocquet, G. Brebec, Y. Limoge, in: R.W. Cahn, P. Haasen (Eds.), Physical Metallurgy, Elsevier, 1996, p. 535, Chapter 7.
[34] K.-H. Robrock, Mater. Sci. Forum 15 (1987) 537.
[35] A. Barbu, G. Martin, Solid State Phenom. 30 (1993) 179.